THE LIMITS OF LOW TEMPERATURE SUPERPLASTICITY IN AA 5083 PRODUCED BY ACCUMULATIVE ROLL BONDING (ARB)

Brady N.L. McBride*[1], Amy. J. Clarke[1], Kester D. Clarke[1]

*corresponding author, bmcbride@mines.edu
[1]Colorado School of Mines George S. Ansell Department of Metallurgical and Materials Engineering
1500 Illinois Street Golden, CO 80401

Keywords: accumulative roll bonding, superplasticity, low temperature

ABSTRACT

Accumulative roll bonding (ARB) is a severe plastic deformation technique used to produce microstructures conducive for low temperature superplasticity. This processing technique not only produces sub-micron grains but also non-equilibrium grain boundaries with increased grain boundary diffusivity. Low temperature superplasticity ($225<T<250$°C) was achieved with activation energies between 40 and 80 kJ/mol; significantly lower than what is commonly reported for grain boundary sliding limited by grain boundary diffusion (84 kJ/mol). This reduction in activation energy is a direct result of non-equilibrium grain boundary development which allows for enhanced diffusion rates at substantially lower temperatures. Activation energies increased above 100 kJ/mol after 15 minutes of thermal exposure between 225 and 250°C, providing further evidence that low temperature superplasticity relies heavily on the metastable grain boundary structure produced by ARB. The cavitation void area fraction for optimal low temperature superplastic conditions was well below 1% for thinning ratios (t_o/t_f) around 2.0 (ε=0.75, e=1.12), which is far superior compared to the ≈5% achieved in conventionally processed material (T=500°C) strained to similar levels. This work not only provides a framework for the temperature and strain rate limits of superplasticity of submicron grained material, but also investigates critical parameters pertinent to the forming industry, including damage accumulation, strain localization and thermal stability of microstructure.

INTRODUCTION

Developments in superplastic sheet forming have led to the production of complex geometries from monolithic sheets that would be otherwise impossible using traditional forming methods such as stamping, bending or drawing [1,2]. Superplastic forming has the additional benefit of reducing the overall numbers of parts and fasteners involved in an assembly, thus reducing the total weight [1,2]. A prime example of this is seen in the 2018 Bentley GT Continental, the first automobile to have all of its outer paneling produced with superplastic forming, contributing to an overall 85 kg weight reduction in the body structure [3]. Similar adaptations are being made in the aerospace industry for non-structural enclosures [1,4]. Despite these benefits, superplastic forming possesses its

own limitations. Superplasticity typically requires high forming temperatures and low strain rates which result in high operating costs and long cycle times; this limits the profitability of superplastic forming to low volume, high value-added part manufacturing [1,4-6]. Novel thermo-mechanical processing techniques have demonstrated low temperature superplasticity [7,8], which has the potential to reduce costs associated with forming conventional superplastic alloys such as AA 5083.

AA 5083 (Al-4.4Mg-0.7Mn) is a work-hardenable alloy which makes use of Mg solute additions and fine dispersoids to reduce the propensity for recovery and to retain strain energy [6,9]. Recrystallization heat treatments after deformation produce a refined microstructure with grains on the order of 10 μm, which exhibits superplasticity at temperatures around 500°C and strain rates on the order of 1×10^{-4} s^{-1} [5,6,9,10]. Superplastic strain rates can be modeled by the empirical relationship

$$\dot{\varepsilon} = A\frac{DGb}{kT}\left[\frac{b}{d}\right]^{p}\left[\frac{\sigma}{G}\right]^{1/m} \quad (1)$$

where A is a material constant, D the diffusivity of the rate-limiting deformation mechanism, G the elastic modulus, b the burgers vector, k the Boltzman constant, and d the grain size [11]. The exponents p and m are the grain size exponent and strain rate sensitivity, respectively. Superplasticity generally occurs due to grain boundary sliding with a strain rate sensitivity around 0.5 [5]. The direct relationship between grain size and temperature suggests grain refinement can lead to grain boundary sliding at lower temperatures. Alternatively, it may be possible to achieve higher strain rates at the same temperature. Either of these outcomes has the potential to reduce costs associated with superplastic sheet forming.

Methods of grain refinement in aluminum alloys, particularly AA 5083, have gained notable interest over the past few decades. Severe plastic deformation (SPD) techniques such as high pressure torsion (HPT) [12], equal channel angular pressing (ECAP) [13] and ball-milling [14] are a few examples used to produce grain sizes on the order of a few hundred nanometers. These processing methods are limited by their inability to produce bulk material relevant to industrial-scale forming processes. Continuous deformation processes, such as severe rolling, can produce bulk monolithic material using conventional processing equipment. Severe warm rolling and accumulative roll bonding (ARB) are two methods that have been used frequently to produce ultra-fine grained material [7,8,15].

Severe warm rolling of AA 5083 has been used to produce material with strains as high as 4, resulting in subgrains on the order of 500 nm [7]. Warm rolling is conducted without intermediate static annealing to suppress recovery and recrystallization [7]. The resultant material has been shown to exhibit superplastic tensile elongations on the order of 400% with temperatures and strain rates of 230°C and 1×10^{-3} s^{-1}, respectively [16]. Despite the potential for low temperature superplasticity, this process has its own limitations. To achieve a final strain of 4 in a sheet geometry, the starting material must be on the order of a few centimeters thick. Moreover, employing a series

of rolling passes with different reductions and temperatures increases the susceptibility to undesirable process variability that would be difficult to minimize.

Accumulative roll bonding (ARB) is an alternative to severe warm rolling capable of producing ultra-fine grained sheet material [8,17]. This process involves repeated stacking and roll bonding of two sheets with 50% reduction passes. After each pass the roll-bonded sheet is nominally twice as long and half as thick as the starting geometry; the sheet is then sectioned in half and the process repeated. This process is advantageous over severe warm rolling in that the same reduction is used for each pass, aiding in modeling efforts and process consistency. AA 5083 processed with 5 cycles of ARB (ε=4) leads to grains on the order of 250 nm and has been shown to exhibit superplastic elongations as high as 200% for temperatures of 200°C and strain rates of 1×10^{-3} s^{-1} [18].

Despite early success in demonstrating low temperature superplasticity, additional work is needed to understand the relationship between severely deformed microstructures and mechanical properties. Stress-strain behavior during superplastic deformation is markedly different for samples produced by severe warm rolling as opposed to ARB [16,18]. One possible explanation for this discrepancy is effect of strain path on thermal stability of microstructure due to differences in high angle grain boundary (HAGB) fraction [19]. Furthermore, while previous studies have suggested optimal parameters for superplasticity [13,16], these parameters have not been finalized or rationalized in terms of acting deformation mechanisms. Previous reports on superplasticity of sub-micron grained microstructures are further confounded by a lack of standardized testing parameters, such as heating rate and soak duration of samples prior to elevated temperature testing [18,20]. Little, if any, discussion has taken place concerning the effects of prolonged thermal exposure on microstructural stability during superplastic forming. Lastly, microstructural characterization after forming, including final grain size, cavitation damage and strain uniformity, has yet to be fully explored in the context of optimizing a cost-saving low temperature superplastic response.

Previous work by the authors lead to the development of a reliable and consistent ARB process to produce bulk samples without deleterious edge cracking [17]. This allowed for thorough investigation of the thermal stability of AA 5083 microstructures produced with ARB to suggest possible temperature limits for low temperature superplasticity [15]. The present work continues to investigate the industrial applicability and limitations of low-temperature superplasticity through a holistic examination of the acting deformation mechanisms, optimal temperature and strain rate combinations and microstructural damage that occurs during uniaxial tensile testing.

METHODOLOGIES

Plates of 3.2 mm thick AA5083-H116 were used as starting material with composition listed in Table 1. Plates were solutionized at 500°C for 30 minutes, cold rolled with a 68% reduction to 1 mm and then statically recrystallized at 500°C for an additional 30 minutes before being water quenched. ARB was conducted using single 50% reduction passes with unlubricated rolls for a total of 5 cycles. Samples were preheated in an air furnace at 250°C prior to each roll bonding cycle to reduce flow stress and encourage bonding; preheating time was limited to 5 min to avoid strain recovery. Sacrificial aluminum frames as discussed in [17] were used to mitigate edge cracking associated with lateral spreading. All rolling was conducted on a two-high laboratory scale Fenn rolling mill with 133 mm rolls operating at 37 RPM. The microstructure after ARB processing had grain sizes between 250 and 500 nm and a HAGB fraction around 0.8, as previously reported [15].

Table 1 Composition of as-received AA 5083 (wt. %).

Mg	Mn	Cr	Cu	Fe	Si	Ti	Zn	Al
4.32	0.44	0.06	0.04	0.30	0.11	0.01	0.07	bal

Tensile samples were machined with a 12.7 by 6.4 mm gauge section. The gauge length was parallel to the rolling direction and had a 1.6 mm transition radius between the grip and gauge section. A gauge length smaller than that recommended by ASTM E2448 (25.4 mm) was used to minimize thermal gradients along the sample at high strains. Specialized grips were used to transfer load to the specimen shoulders and minimize errors associated with material flow [21]. Tensile testing was conducted on a screw-driven load frame equipped with a 4.4 kN load cell and pull-rods extending into a 3-zone clamshell air furnace. Samples were given 15 minutes prior to the start of each test to reach thermal equilibrium with the load train and furnace, which were held at the testing temperature. Temperature along the gauge length was found to be consistent within ±3°C prior to the start of each test. All tests were conducted using true strain rate control by adjusting the crosshead velocity as a linear function of displacement. Strain rates ranging from 2×10^{-4} and 5×10^{-3} s^{-1} were investigated. True strain calculations assumed constant uniform thinning and volume constancy. Frame deflection under maximum load was measured to be less than 1% of the original gauge length, and crosshead displacement was taken as a direct measure of tensile elongation.

Strain rate jump tests were used to determine strain rate sensitivities as shown in Figure 1. Samples were first deformed to a true strain of 0.15 before the strain rate was increased by 20%. Deformation proceeded at this increased rate for an additional 0.1 strain, at which point the strain rate was decreased back to the original rate. This cycle was repeated for every 0.1 strain increment until failure. This method was chosen to observe the evolution of strain rate sensitivity as a function of strain while minimizing the amount of microstructural evolution associated

with large strain rate changes [22]. The steady-state stress values corresponding to each strain rate jump were determined by extrapolating local flow data to the start of the jump.

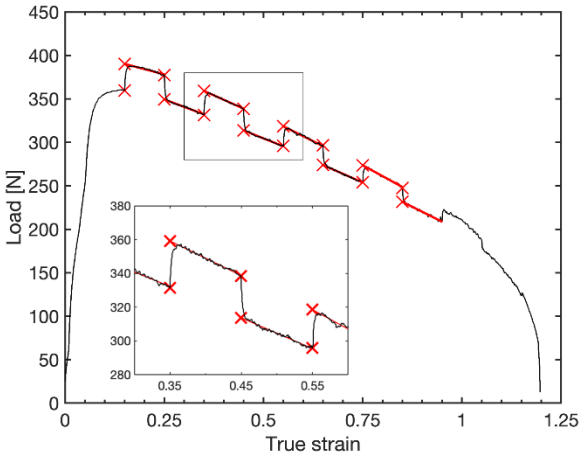

Figure 1 Example flow curve from a strain rate jump test (*ARBed* condition, 250°C, 5×10^{-4} s^{-1}) showing the method used to determine strain rate sensitivity, *m*. True strain rate is incrementally increased and decreased by 20% every 0.1 true strain until failure. Crosses mark extrapolated load values used in calculation.

Electron backscatter diffraction (EBSD) analysis was performed on a JEOL 7000 JSM-7000F field emission scanning electron microscope (SEM) operating at 15 kV with an EDAX Hikari Pro detector. EBSD data was processed with EDAX's Neighbor Pattern Average and Reindexing (NPAR) software to increase Kikuchki pattern fidelity in highly strained regions and then further refined using a neighbor orientation correlation (NOC) algorithm with a cleanup level of '5', minimum confidence index of 0.1 and 2° orientation threshold. Samples for EBSD analysis were mounted in a low-temperature epoxy resin, ground and polished in incremental steps and then electropolished using Struers A2 electrolyte at 39 V for 5 seconds at room temperature.

Microstructural damage during uniaxial tensile testing was characterized using an image analysis routine on backscatter electron (BSE) micrographs of the longitudinal plane of samples. A contrast threshold was applied to BSE micrographs to delineate voids from the surrounding microstructure. ImageJ's Analyze Particles routine was used to measure the size and shape of voids. A resolution of 0.1 µm/pixel was used and only voids consisting of four neighboring pixels were included in calculations. Spatial summation (e.g. along the rolling/tensile direction) of void pixels was employed to create void intensity profiles through-thickness.

A 15 minute static annealing heat treatment at either 240 or 250°C was given to a subset of samples to investigate the effects of thermal microstructural stability on superplastic performance. This was prior and in addition to the 15 minutes used to preheat samples to the furnace temperature. Static annealing temperatures were specially chosen to promote continuous recrystallization while avoiding deleterious grain growth that occurs above 250°C [15]; subsequent tensile testing on these partially recrystallized samples was conducted at or below 250°C. The thermal processing history of these different starting microstructures is shown schematically in Figure 2. The

different microstructural conditions tested will hereafter be referred to as the *ARBed* (Figure 2a), *240RX* (Figure 2b) and *250RX* (Figure 2b) conditions.

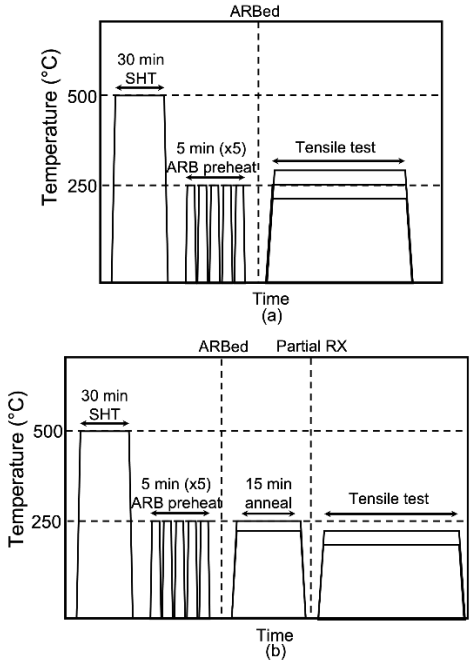

Figure 2 Schematic showing thermal processing history for the (a) *AsARBed* and (b) partially recrystallized microstructures. The partially recrystallized samples (*240RX* and *250RX*) received a 15 minute static annealing heat treatment at 240 and 250°C, respectively, prior to tensile testing. Note 15 minutes of preheating time was applied to each sample immediately preceding tensile testing, regardless of previous static annealing treatments.

Microstructures of the three different microstructural conditions preceding tensile testing are shown in inverse pole figure (IPF) maps in Figure 3. The location of these microstructures in the thermal processing history schematic (Figure 2) is designated as either *ARBed* or *Partial RX*. Short duration static annealing at low temperatures has a marked effect on the morphology of grains with a change in the elongated deformation structure after exposure at 240°C. The microstructure after 250°C exposure is similar albeit with near-equiaxed grains and evidence of grain growth. TEM micrographs shown in Figure 4 provide additional information about the dislocation density and grain boundary structure of the different microstructures. The *ARBed* condition appears to consist of grains with higher dislocation densities and only partially resolved grain boundaries. In the *240RX* and *250RX* conditions the dislocation density appears lower and grain boundaries are more distinct. This microstructural transition has been attributed to continuous dynamic recrystallization and has been previously reported by the authors in extensive detail [15].

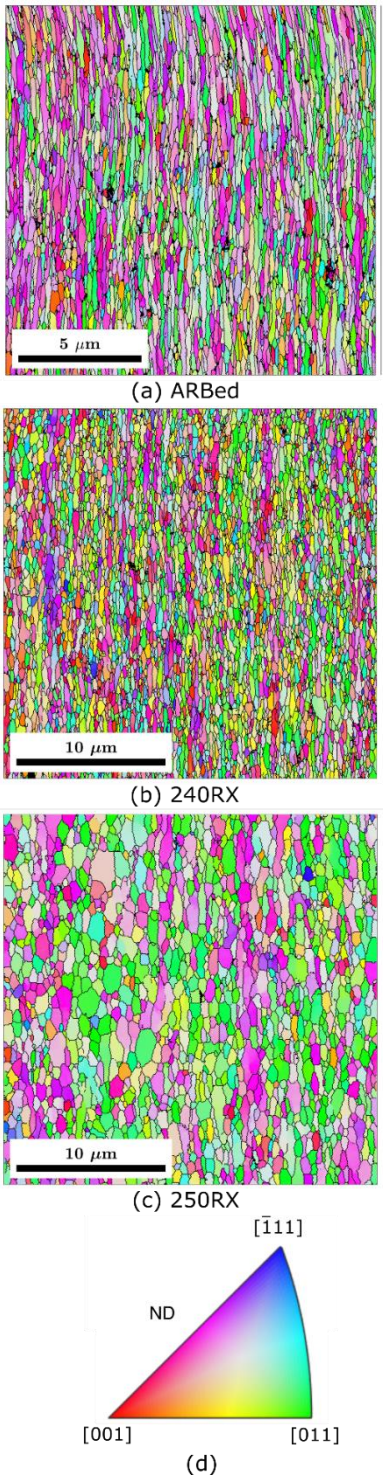

Figure 3 Inverse pole figure (IPF) maps of the longitudinal plane near the sample mid-thickness showing grain morphology for the (a) *ARBed*, (b) *240RX* and (c) *250RX* conditions preceding tensile testing. Note the change in scale bar between maps. The rolling direction is vertical and the normal direction is horizontal. Grain orientations are colored with respect to the normal direction in (d).

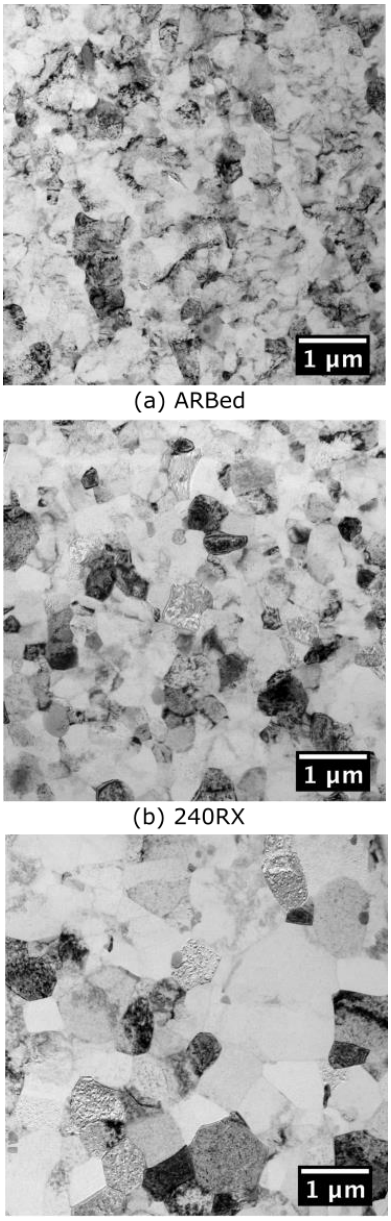

Figure 4 TEM brightfield micrographs from the rolling plane taken near the mid-thickness of samples showing dislocation density and grain boundary character for the (a) *ARBed*, (b) *240RX* and (c) *250RX* conditions. The rolling direction is vertical and the transverse direction is horizontal.

EFFECTS OF PARTIAL RECRYSTALLIZATION ON SUPERPLASTICITY

Total tensile elongations for the three different starting microstructures (Figures 3 & 4) tested under various temperature and strain rate combinations are shown in Figure 5. There is a clear dependence of microstructure on elongation to failure despite all microstructures having initial sub-micron grain sizes. The *ARBed* microstructure achieved tensile elongations as high as 275%, whereas the *240RX* and *250RX* conditions only achieved as much as 125%. In all cases, total tensile elongation increases with decreasing strain rate, with the

ARBed condition being substantially more sensitive to strain rate. Attention should be drawn to the fact that tensile elongation does not scale linearly with strain rate; instead, the marginal increases in ductility become less with each reduction in strain rate. This suggests some sort of trade-off between maximizing formability (total tensile elongation) and minimizing forming cycle time (strain rate), which will be discussed in more detail in the following sections. The depreciation of total tensile elongation with decreased strain rate is also indicative of a transition to regime I creep [5].

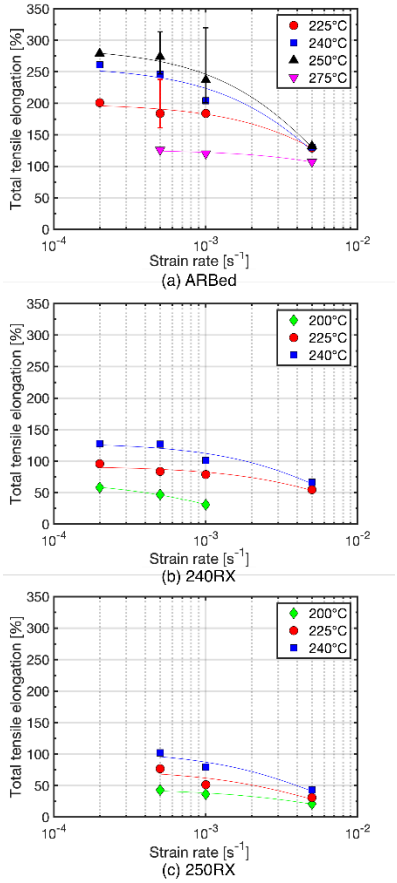

Figure 5 Total tensile elongations for the (a) *ARBed*, (b) *240RX* and (c) *250RX* microstructural conditions. Error bars are used in cases where duplicate samples were tested. Large discrepancies in duplicate samples are due to the formation of multiple diffuse necks preceding failure. Tests were duplicated until a sample that failed with one diffuse neck was achieved for a direct comparison.

The effect of temperature on superplastic ductility is not as straightforward. At first glance total tensile elongation increases with temperature. In the *ARBed* condition, an increase in temperature from 225 to 250°C (ΔT=25°C) is responsible for an additional 50 to 75% elongation. This effect of temperature is not exhibited to the same extent in the *240RX* and *250RX* conditions, where an increase in temperature from 200 to 240°C (ΔT=40°C) results in only a 50% increase in elongation. On the other hand, the effect of raising temperature above 250°C is

highly consequential; a temperature increase from 250 to 275°C (ΔT=25°C) results in a roughly 100% decrease in elongation for the *ARBed* condition. The *240RX* and *250RX* conditions were not tested at higher temperatures, but it is interesting to note that testing at 275°C for the *ARBed* condition fared worse than testing at 240°C for the partially recrystallized conditions. Previous work by the authors [15] has shown significant grain growth to occur above 250°C, and it has been suggested that grain growth is not conducive for grain boundary sliding [16]. Thus, deformation at 250°C may be an upper limit for low temperature superplasticity.

Strain rate sensitivities calculated via strain rate jump tests for the three microstructures provide further information about the mechanisms responsible for superplasticity. Figure 6 shows a parabolic relationship between strain rate and strain rate sensitivity which is typical of materials deforming under creep conditions [5]. A maximum strain rate sensitivity (m≈0.5) due to grain boundary sliding typically occurs at intermediate strain rates in superplastic materials; this is referred to as regime II creep [5]. The location of this maximum is consistently between strain rates of 5×10^{-4} to 1×10^{-3} s^{-1} independent of starting microstructure. This is in agreement with other studies on both coarse-grained [10,23] and sub-micron grained [18,24] AA 5083 tested at temperatures around 500 and 250°C, respectively. It should be noted, however, that the strain rate sensitivity for sub-micron grained material reportedly tends toward 0.3 for strain rates below 1×10^{-4} s^{-1} [18,24], whereas coarse-grained material typically retains high strain rate sensitivities (m≈0.4) for strain rates as low as 1×10^{-5} s^{-1} [10,23]. Overall, the strain rate sensitivities of the *ARBed* microstructure showed the least dependence on temperature. Error bars in Figure 6 show the range of strain rate sensitivities observed during deformation for each condition tested. Strain rate sensitivities generally start high and decay with increased strain, thus providing an indirect measure of microstructural evolution during testing.

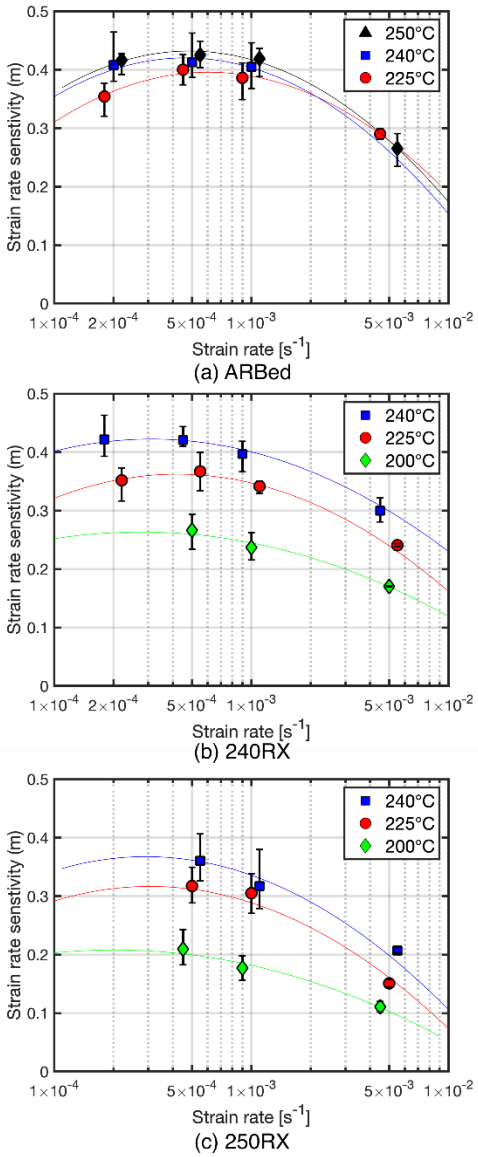

Figure 6 Strain-rate sensitivity (m) values for the (a) *ARBed*, (b) *240RX* and (c) *250RX* microstructural conditions calculated using a repeated strain rate jump test. Error bars represent the range of strain rate sensitivities observed during deformation.

Additional information concerning deformation mechanisms can be ascertained by calculating activation energies. The activation energy for deformation represents the change in stress resulting from a change in temperature through the relationship

$$Q = \frac{k}{m}\frac{\delta \ln \sigma}{\delta\, 1/T}\bigg|_{\varepsilon,\dot{\varepsilon},d} \tag{2}$$

which is a rearrangement of Equation 1. A graphical example of how activation energies are calculated is shown in Figure 7 and activation energies for different testing parameters are shown in Figure 8. Note Equation 2 assumes a constant grain size and microstructure, limiting this analysis to temperature and strain rate combinations

demonstrating similar (m±0.05) strain rate sensitivities. For the *250RX* condition, activation energies are near self diffusion in aluminum (Q_{Al} = 142 kJ/mol [9]) with some variation to lower energies around 120 kJ/mol. The *240RX* condition also exhibits mean activation energies around Q_{Al}, albeit with a greater tendency toward values between 100 and 120 kJ/mol. While these values are still much higher than that of grain boundary diffusion in aluminum typically associated with superplasticity (Q_{GB} = 84 kJ/mol [9]), their respective m values, between 0.3 and 0.4, are also considerably higher than that of diffusional creep (m=0.2) [5,9]. This suggests deformation consisting of both grain boundary sliding and diffusional creep, with the accommodation by diffusional creep being greater in the *250RX* condition.

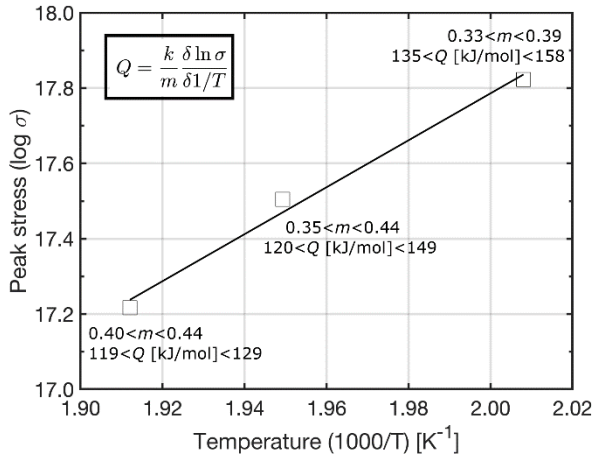

Figure 7 Example showing the calculation of activation energy from peak stress and temperature for samples deformed in the ARBed condition at 2×10^{-4} s^{-1}. A linear regression is conducted between peak stress and temperature; ranges of strain rate sensitivities (Figure 6) are used to calculate activation energies at each temperature.

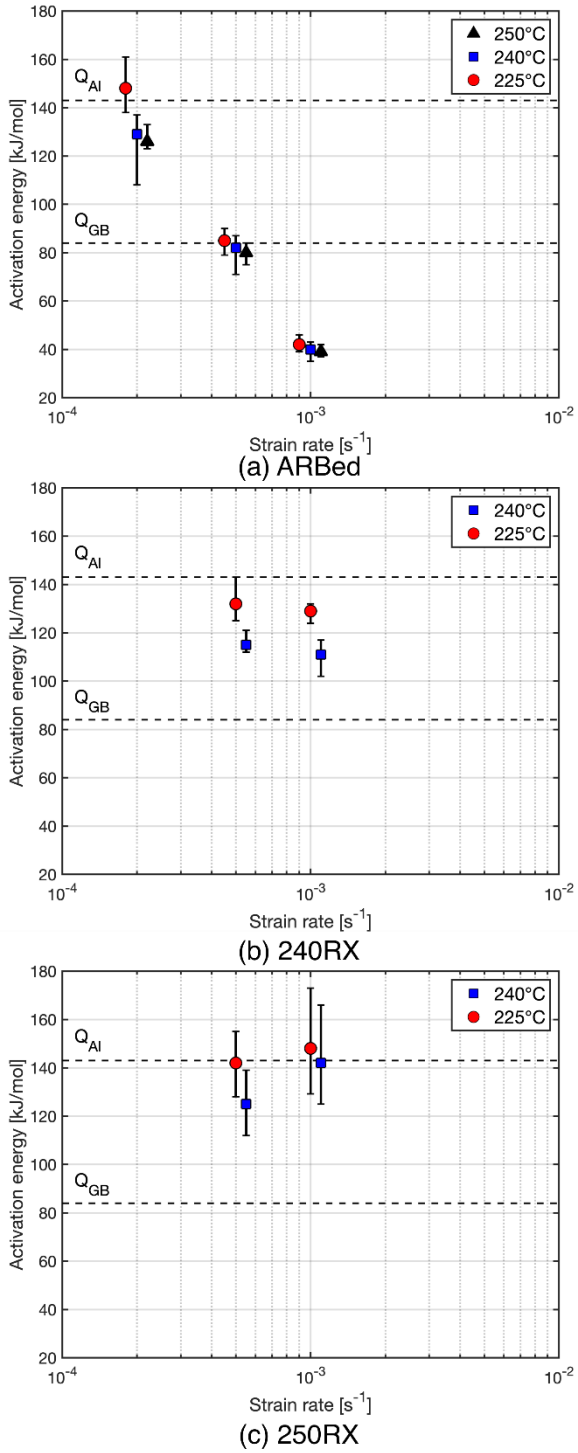

Figure 8 Activation energies for the (a) *ARBed*, (b) *240RX* and (c) *250RX* microstructural conditions. Error bars represent the range of activation energies calculated from the evolution of strain rate sensitivity observed during deformation.

The activation energies for the *ARBed* condition are considerably different than those for the partially recrystallized conditions. Activation energies as low as 40 kJ/mol are observed at 1×10^{-3} s^{-1}. More confounding still is that activation energies are near that of grain boundary diffusion for 5×10^{-4} s^{-1} but then continue to increase with

decreasing strain rates toward 2×10^{-4} s^{-1}; all of these instances occur with strain rate sensitivities indicative of grain boundary sliding (0.4<m<0.5). This will be the subject of future discussion in a following section.

CHARACTERIZATING OPTIMAL SUPERPLASTIC RESPONSE

Two testing conditions (5×10^{-4} s^{-1} at 225°C and 1×10^{-3} s^{-1} at 250°C) with the *ARBed* microstructure were investigated in more detail to determine the cause of low activation energies associated with grain boundary sliding (0.4<*m*<0.5). Although both conditions exhibited tensile elongations in excess of 200% and strain rate sensitivities above 0.4, they possessed significantly different mean activation energies — around 82 and 40 kJ/mol, for the low and high strain rate conditions, respectively.

Inverse pole figure (IPF) maps showing microstructural evolution with strain are shown in Figure 9. Note these are colorized with respect to the RD as opposed to the conventional ND shown in Figure 2, to provide greater distinction between texture components with similar plane normals, such as Brass {011}<211> and Goss {110}<001>. A microstructural transition occurs at low strains (ε<0.1) which results in a finer microstructure compared to immediately after static annealing (Figure 3). This is akin to continuous dynamic recrystallization, which may be energetically favorable at low strain levels if the initial microstructure consists of a significant proportion of remnant subgrains. Subgrains rely on cooperative grain boundary sliding (CGBS) rather than independent grain boundary sliding, which may increase the driving force for subgrain boundary mobility [25, 26]. Continuous geometric dynamic recrystallization (GDRX) may also be active, where HAGBs "pinch off" elongated grains under the influence of an applied tensile stress in the rolling direction [27].

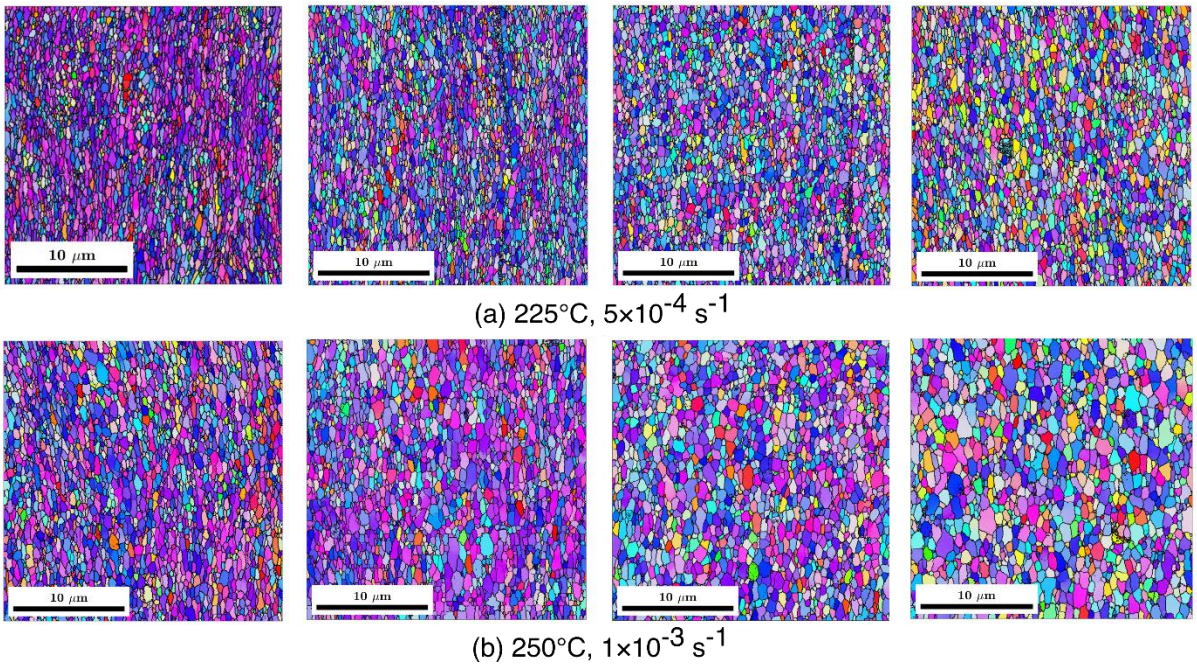

Figure 9 Inverse pole figure (IPF) maps of the longitudinal plane taken near the mid-thickness after interrupted tests at 0.1, 0.25, 0.5 and 0.75

true strain for the *ARBed* microstructure tested at (a) 225°C, 5×10^{-4} s^{-1} and (b) 250°C, 1×10^{-3} s^{-1}. The rolling and tensile directions are vertical while the normal direction is horizontal. IPF orientations are with respect to the rolling direction.

This initial dynamic recrystallization may explain the difference in work-hardening behavior between material produced with severe warming rolling and ARB [16,17]. Severely warm rolled material exhibits extensive work hardening up to approximately 0.5 true strain (e=0.65) [7,28] after which there is a sharp decrease in the cluster size of regions participating in CGBS [16]. On the other hand, *ARBed* material only strain hardens until approximately 0.1 true strain (e=0.11) [18]. While the nature of CGBS in material produced with ARB has yet to be discussed in literature, the greater fraction of HAGBs in *ARBed* material (≈0.8) [15] compared to severely warm rolled material (≈0.4) [16] suggests *ARBed* material exhibits a faster transition from CGBS to independent GBS during early stages of deformation. Thus, processing pathways may have a marked effect the degree of dynamic recrystallization at low strains, which have the potential to culminate in significance differences in subsequent superplastic deformation behavior. While this topic is of notable interest for optimizing a superplastic response, it is outside the scope of this work and will not be discussed in more detail.

The stress-strain curves of the two testing conditions are presented in Figure 10 with strain rate sensitivity (m) and work hardening coefficient ($\gamma = d\varepsilon(d\sigma/d\varepsilon)$ values overlaid. Work hardening coefficients were calculated from engineering stress and do not account for cross-sectional area reduction. Both conditions exhibit stable grain boundary sliding as evidenced by the high strain rate sensitivities ($0.4<m<0.5$) sustained for the majority of deformation. The operation of grain boundary sliding is further corroborated by the interrupted strain IPF maps shown in Figure 9. Grain size and morphology remain constant up to 0.75 true strain (e=1.12) with a general weakening of texture, neither of which would occur during dislocation-creep deformation.

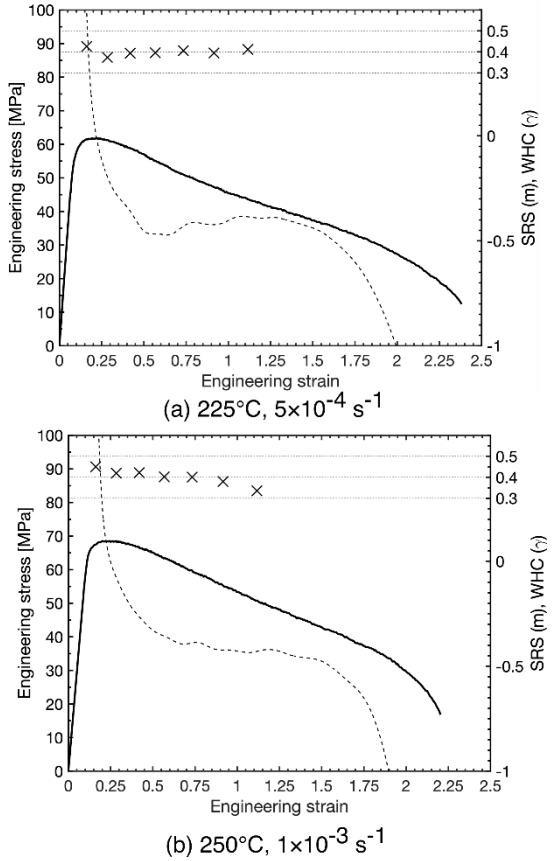

Figure 10 Engineering stress-strain curves for *ARBed* material tested at (a) 225°C, 5×10^{-4} s^{-1} and (b) 250°C, 1×10^{-3} s^{-1}. The dashed line represents the instantaneous work hardening coefficient (WHC), γ, while the crosses represent strain rate sensitivity (SRS), m. Stable grain boundary sliding is apparent in both conditions until the point of final strain localization, which occurs around roughly 1.0 true strain (e=1.72) as evidenced by the local plateau in work hardening coefficient.

Deformation at strain levels greater than 0.75 (e=1.12) progresses with accelerated strain localization. This is shown in Figure 11, which summarizes the thinning ratio (t_o/t_f) along the gauge length for different bulk strain levels. Perturbations in the thinning ratio for strains less than 0.75 (e=1.12) are indicative of necks that localize and strain-rate-harden during deformation; these are responsible for fluctuations in the γ curves in Figure 10. A transition from quasi-uniform to localized strain occurs between 0.75 and 1.0 strain (e=1.12 and 1.72) for both conditions which manifests as a drop in strain rate sensitivity and local plateau in the work hardening coefficient. Strain localization in the final neck contributes an additional 75% elongation when tested at 250°C, 1×10^{-3} s^{-1} (m≈0.42) compared to an additional 100% for 225°C, 5×10^{-4} s^{-1} (m≈0.40). Evidently, deformation is more uniform at 250°C, 1×10^{-3} s^{-1} due to the higher strain rate sensitivity.

Damage accumulation in the microstructure in the form of cavitation voids was characterized through-thickness using image analysis on backscatter scanning electron micrographs. Spatially-resolved void intensity profiles through thickness, where void intensities are summed along the rolling (tensile) direction, are shown in Figure 12 for different strain levels. Void intensities appear at regular intervals through thickness which correspond

to the individual bonding interfaces. Void presence is minimal for both testing conditions up to 0.75 strain (e=1.12) with mean void sizes below 1 μm in diameter. The void size and area fraction increase at higher strains with void growth significantly faster at 225°C. The void profiles in Figure 12 correlate well to the strain localization in Figure 11; the two conditions exhibit extensive strain localization and void formation above 0.75 strain (e=1.12), although both characteristics are more extreme at 225 °C.

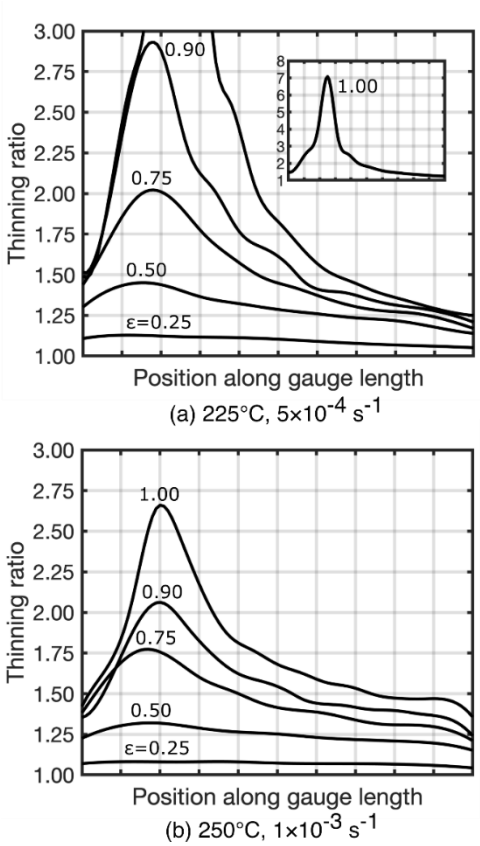

Figure 11 Thinning ratios (t_o/t_f) measured along the gauge length at different strain levels for the *ARBed* condition tested at (a) 225°C, 5×10^{-4} s^{-1} and (b) 250°C, 1×10^{-3} s^{-1}. True strain values reported are of the bulk sample assuming uniform elongation.

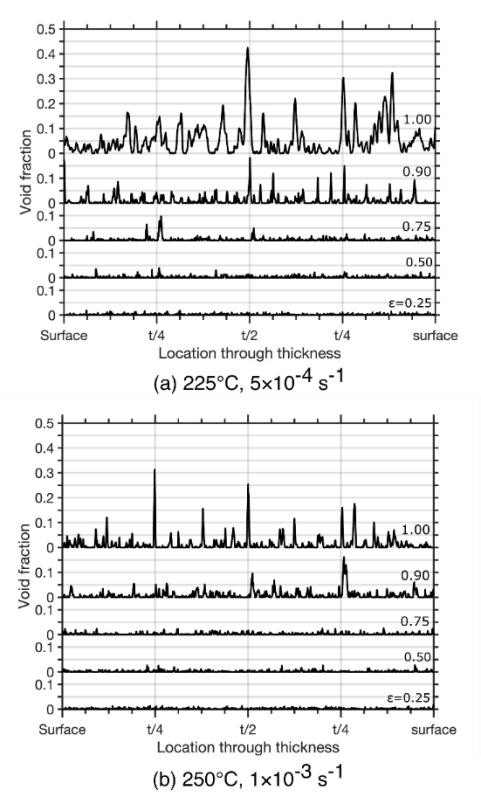

Figure 12 Through-thickness void intensity profiles summed along the rolling/tensile direction for the *ARBed* condition tested at (a) 225°C, 5×10^{-4} s^{-1} and (b) 250°C, 1×10^{-3} s^{-1}. Void intensities become prominent after 0.75 strain (e=1.12) and are more severe for testing at 225°C.

DISCUSSION

Total tensile elongation has proven to be highly dependent on microstructure, temperature and strain rate for sub-micron grained material produced with ARB. As with most SPD techniques, the microstructure after processing consists of non-equilibrium grain boundaries characterized by high free volume [29]. These boundaries arise from the vast amount of intrinsic grain boundary dislocations that are introduced during processing, which increase the boundary energy without contributing to misorientation [29]. Such non-equilibrium grain boundaries are two to four times wider than a traditional HAGB, which results in enhanced grain boundary diffusivities and lower activation energies for grain boundary diffusion [30–32].

The presence of non-equilibrium grain boundaries partially explains the deformation behavior observed with different starting microstructures. Grain boundary sliding ($0.4<m>0.5$) in the *ARBed* condition at strain rates above 5×10^{-4} s^{-1} occurs with activation energies much lower than those reported for diffusion in conventional grain boundaries – between 40 to 80 kJ/mol compared to 84 kJ/mol. This reduction in activation energy is attributed to enhanced diffusion along non-equilibrium grain boundaries. Grain boundary sliding is also presumed to occur for the *240RX* and *250RX* microstructures for temperatures and strain rates between 225 to 240°C and 5×10^{-4} to 1×10^{-3},

respectively; the activation energies (<143 kJ/mol) and m values (0.35 to 0.45) are in the appropriate range for this type of deformation. The increase in activation energy for the partially recrystallized microstructures is associated with grain boundary recovery, where the non-equilibrium nature of boundaries is lost and grain boundary diffusivities tend toward conventional values. It should be noted that grain boundary sliding is not an independent deformation mechanism, but rather a combination of creep mechanisms relying on bulk and grain boundary diffusion. Thus, instances where activation energies are closer to Q_{Al} than Q_{GB} suggest a greater proportion of lattice diffusion accommodation mechanisms. A similar argument can be made for strain rate sensitivities; while m values of 0.5, 0.3 and 0.2 are generally associated with pure grain boundary sliding, solute drag creep and dislocation creep [5], respectively, intermediate values suggest a combination of deformation mechanisms.

Superplastic behavior, using the definition of m>0.3 and elongation of at least 200% [5], is not observed for any of the microstructures tested below 225°C. Deformation of the partially recrystallized microstructures at 200°C occurs with strain rate sensitivities (m<0.25) indicative of dislocation creep. Although the *ARBed* microstructure was not tested below 225°C, extrapolation to lower temperatures suggests deformation would likely occur with strain rate sensitivities around 0.3 and tensile elongations not exceeding 150%. Thus, it is concluded that grain boundary sliding is not a dominant deformation mechanism below 225°C, likely due to reduced thermal mobility. This raises the question of using lower strain rates to compensate for reduced thermal mobility at lower temperatures.

The effect of lower strain rate on tensile properties is particularly interesting, as rates below 5×10^{-4} s^{-1} correlate with both higher tensile elongations and activation energies. In the *ARBed* condition, strain rates of 2×10^{-4} s^{-1} produce m values indicative of grain boundary sliding (0.35<m<0.45) but also activation energies suggestive of dislocation creep (108 to 160 kJ/mol). This can be explained in terms of solute-dislocation interactions in solid solution strengthened alloys. As strain rate decreases, so does the resolved shear stress on the crystal lattice and therefore the velocity of mobile lattice dislocations [33, 34]. At elevated temperatures solute atoms, which are attracted to the dislocation strain fields, have enhanced thermal mobility. The combination of these factors means the dislocation velocity is comparable to the velocity of diffusing Mg atoms, which results in a drag force on dislocation motion [32, 33]. This phenomenon is commonly referred to as solute drag creep (m=0.3) [5], where deformation is rate-limited by the diffusion of solute and demonstrates an activation energy near that of Mg diffusion in Al (Q_{Mg}=136 kJ/mol) [33-35]. This hypothesis is supported by other studies in literature; solute drag has been postulated as a primary deformation mechanism in other sub-micron AA 5083 studies [16], and a transition from dislocation creep to solute drag creep, independent of grain size, has been observed for strain rates below 1×10^{-3} s^{-1} in Al-Mg alloys [35]. Thus, a transition from grain boundary sliding (0.4<m<0.5) to solute drag creep (m≈0.3) occurs at lower strain rates below 5×10^{-4} s^{-1}.

To further discuss the effects of temperature on active deformation mechanisms, bulk and grain boundary diffusivities for pure aluminum are reported in Table 2 with respect to the length scale of the Burgers vector (b^2/t)

and grain size (d^2/t) [9]. For the temperature range of interest — 200 to 250°C —bulk diffusivity is sufficient for diffusion on the scale of the Burger's vector but not high enough to traverse the grain interior (i.e. $b^2/t < D_{bulk} < d^2/t$). Appreciable diffusion is therefore limited to short circuits along grain boundaries and in the narrow mantle region that extends from grain boundaries toward the grain interior [36]. Some studies have suggested bulk diffusion in the narrow region of the mantle to be considerably faster than bulk diffusion through the lattice, with levels similar to that of grain boundary diffusion [29,37]. Additionally, appreciable segregation of Mg to the mantle region has been reported in severely deformed Al-Mg alloys [38], which may be an exacerbating factor to the aforementioned solute-drag interactions at low strain rates. Based on the diffusivity values at low temperatures, it becomes clear that deformation accommodation is highly dependent on the structure and composition mantle region.

Table 2 Grain boundary and bulk lattice diffusivities in coarse-grained aluminum as a function of temperature compared to the scale of the Burgers vector, b^2/t and the scale of the grain diameter, d^2/t. A grain size of 500 nm was used to represent the grain scale.

	Temperature [°C]		
	200	225	250
D_{GB} [m^2/s]	3×10^{-13}	6×10^{-13}	1×10^{-12}
D_{bulk} [m^2/s]	4×10^{-19}	2×10^{-18}	8×10^{-18}
b^2/t [m^2/s]		8.2×10^{-20}	
d^2/t [m^2/s]		2.5×10^{-13}	

Experimental data from the tests conducted at 225°C, 5×10^{-4} s^{-1} and 250°C, 1×10^{-3} s^{-1} were compared to several proposed models for grain boundary sliding, shown in Figure 13. These models were populated with experimentally determined stresses, grain sizes, and strain rate sensitivities along with tabulated values of elastic modulus, Burger's vector and relevant diffusivities. All models predict strain rates orders of magnitude lower than what was experimentally observed. Models based on lattice diffusion, such as those by Ashby-Verrall [39] and Langdon [40], fared significantly worse than models based on grain boundary diffusion such as that by Gifkins [36]. It should be noted, however, that strong agreement with the Gifkins model is achieved when the grain boundaries are assumed to be non-equilibrium and modeled as

$$D_{GB} = 5 \times 10^{-12} e^{\left(\frac{-Q}{RT}\right)} \quad (3)$$

with the value of Q taken as 60 kJ/mol (an average of the two conditions based on data in Figure 5) and a grain boundary width, δ, taken as four-times the typical value of 0.5 nm [29,41,42]. This enhanced diffusivity is roughly two orders of magnitude greater than the tabulated values reported in Table 2. Agreement between experimental data and the modified Gifkins model demonstrates the necessity of non-equilibrium grain boundaries in achieving low temperature superplasticity.

The preceding discussion has focused on effects of microstructure, temperature and strain rate on total tensile elongation; the remainder of this section will explore the formability potential of the *ARBed* microstructure

at 225°C, 5×10^{-4} s^{-1} and 250°C, 1×10^{-3} s^{-1}. In particular, forming characteristics of sub-micron grained material will be compared with conventional coarse-grained (10 μm) material.

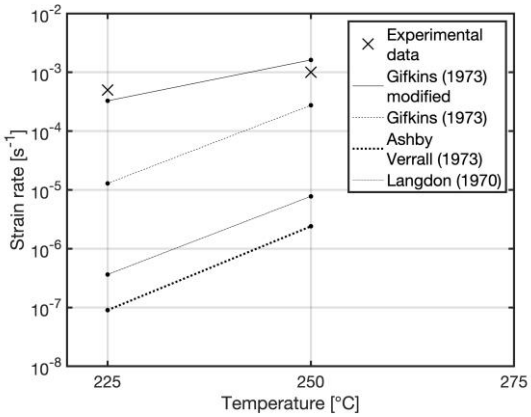

Figure 13 Comparison of experimental strain rates and calculated strain rates from different grain boundary sliding models. All models resemble some form of Equation 1 with appropriate strain rate sensitivities and activation energies.

The *ARBed* microstructure demonstrated stable grain boundary sliding for a significant portion of deformation during both testing conditions, as seen from the microstructural changes in the IPF maps of Figure 9, the stable strain rate sensitivities in Figure 10 and the inhibition of localized necking in Figure 11. To better understand superplastic forming potential, it is worth discussing the mechanisms by which materials fail. Materials tested at low homologous temperatures and quasi-static strain rates fail due to strain localization soon after the Considère criterion is met; for superplastic samples this condition is modified to account for strain rate hardening [43] as

$$\gamma + m < 1 \tag{4}$$

where γ is the work hardening coefficient and m is the strain rate sensitivity. Figure 10 shows that this condition is met shortly after 0.1 true strain (e=0.11) and the majority of deformation thereafter manifests as non-uniform elongation due to the high strain rate sensitivity. Deformation proceeds with initiation and retardation of strain localization resulting in fluctuations in the work hardening coefficient. Cavitation voids, which form when the imposed strain rate is too high for deformation accommodation mechanisms, can also be viewed as a tensile instability; this explains why the increased void presence in Figure 12 closely matches strain localization in Figure 11. The onset of final strain localization, Equation 4, depends on the magnitude of the strain rate sensitivity and therefore occurs earlier at 225°C, 5×10^{-4} s^{-1} (m≈0.40) compared to 250°C, 1×10^{-3} s^{-1} (m≈0.42).

Changes in void size and volume fraction provide additional information regarding tensile instability. Figure 14 shows that voids remain under 1 μm for strains below 0.75 (e=1.25), agreeing with models for diffusion-controlled void growth during grain boundary sliding [5]. Further deformation causes strain-controlled void growth [5] for testing at 225°C, 5×10^{-4} s^{-1} but not for 250°C, 1×10^{-3} s^{-1}. These observations are consistent with the strain localization response in Figure 11, where strain localization is retarded more at 250°C, 1×10^{-3} s^{-1} owing to the

higher strain rate sensitivity. It is worth mentioning that strain localization leads to increased local strain rates and reduced local strain rate sensitivities, which further exacerbates the rate of subsequent strain localization.

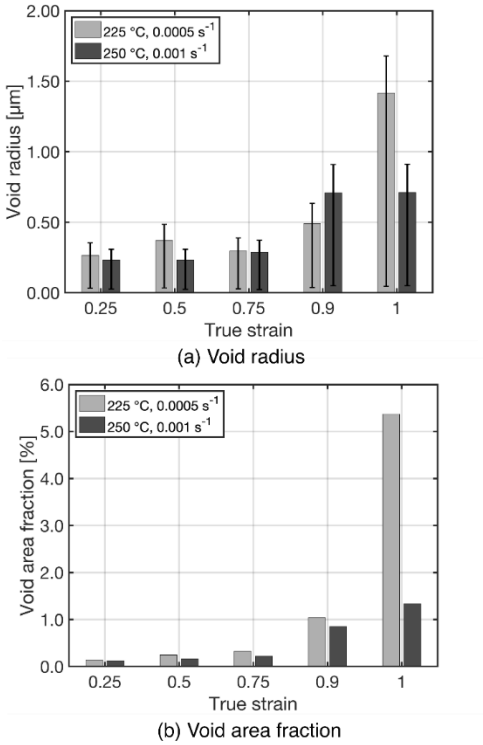

Figure 14 Individual void radius (a) and total void area fraction (b) for the 225°C, 5×10^{-4} s^{-1} and 250°C, 1×10^{-3} s^{-1} conditions as a function of strain. Void size and fraction are stable for both testing conditions below 0.75 true strain (e=1.46).

For current industrial applications, such as the manufacture of automotive body panel discussed initially, superplastic forming is usually limited to thinning ratios (t_f/t_o) < 2 to ensure the cavitation volume fraction does not exceed 2 to 3% [1,4]. The results presented herein suggest thinning ratios as high as 2.5 can be sustained without exceeding 1% void fraction. This is far superior to conventional material (d≈10 μm, T>500°C) strained to similar levels which exhibit void area fractions between 2.5 and 10% [10,23,45]. Attention should be drawn to the fact that void size during grain boundary sliding is generally on the order of the material's grain size [5,10,23,45], which is corroborated by Figure 14. Lastly, void intensities for the *ABRed* material are highest at bonding interfaces, suggesting the bonds are limited in ability to accommodate superplastic deformation, particularly at higher strains. Thus, the *ARBed* material exhibits higher damage tolerance compared to conventional material as the sub-micron grain size and presence of regular interfaces controls the size and distribution of voids.

Grain growth is a final consideration when discussing forming potential, as the grain size after forming correlates with final part strength. Figure 15 shows the change in mean grain size as a function of strain for both testing conditions. The grain growth behavior confirms previous work by the authors [15] where grain size was

found to be stable for extended durations below 225°C. Both forming conditions show apparent grain growth past 0.75 (e=1.12), suggesting a change in grain boundary mobility as a result of strain localization; this may be due to different deformation mechanisms that occur in the localized region prior to failure. Nevertheless, testing at both 225 and 250°C maintains a sub-micron grain size up to 0.75 true strain (e=1.12).

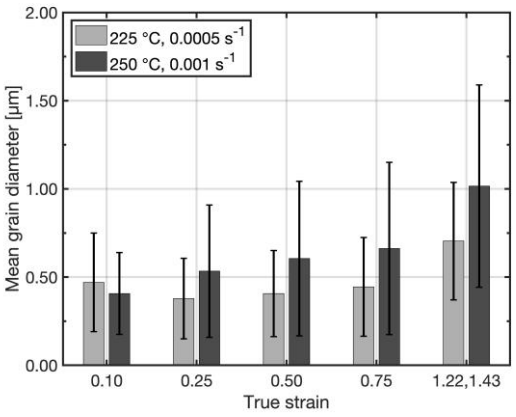

Figure 15 Mean grain diameter at interrupted strains for the ARBed condition tested at 225°C, 5×10^{-4} s^{-1} and 250°C, 1×10^{-3} s^{-1}. Testing at 225°C retains a near-constant grain size, although grain growth occurs immediately preceding failure. Stable grain growth occurs at 250°C as predicted by [11].

CONCLUSIONS

The work presented here outlines the significance of non-equilibrium grain boundaries produced by severe plastic deformation in achieving low temperature superplasticity. Although ARB processing produces sub-micron grains delineated by HAGBs [8,15], it is the excess free volume and high-energy state of these boundaries immediately following severe plastic deformation that reduces the activation energy for grain boundary diffusion. This decreases the energy barrier for grain boundary sliding and allows superplasticity to occur at temperatures as low as 225°C.

The lowest temperature for which grain boundary sliding is operable in severely deformed materials is difficult to identify due to the convoluted interaction between microstructure, temperature and strain rate. While a lower limit of 200°C has been postulated [7,24], this would require even lower strain rates to compensate for the reduction in thermal mobility. This work has shown that strain rates below 5×10^{-4} s^{-1} result in solute drag due to the reduction in dislocation velocity during deformation. Thus, the limiting factor in minimizing the temperature for superplasticity is not the thermal activation for grain boundary sliding, but instead the transition to low strain rate solute drag creep regimes.

The implications of low temperature superplasticity to the sheet forming industry are pronounced. Sub-micron grained material produced by ARB can be deformed to meet current industrial forming limits at a significantly reduced temperature — 225°C ($0.60T_m$) as opposed to 500°C ($0.92T_m$). Moreover, sub-micron grained material has a lower tendency to develop large cavitation voids at appreciable strain levels owing to the reduced grain size; it

may be possible to deform material past current strain limitations without negatively affecting final part strength. A final benefit of material produced with ARB is Hall-Petch strengthening. Grain size remains sub-micron up to 0.75 true strain (e=1.12), meaning final sheet components after forming have the potential to exhibit higher strengths. This may be sufficient to reduce the overall part thickness needed in sheet assemblies.

The benefits that arise from ARB processing all stem from the creation of non-equilibrium grain boundaries during processing. While this work has provides a holistic view of the effects of microstructure, temperature and strain rate on superplasticity, it is evident this behavior is highly dependent on atomic-scale structures of boundaries which are thermally unstable; additional preheating by as much as 15 minutes reduces tensile elongation by a much a 100%. The effect of starting microstructure on superplastic performance was also discussed with comparison to studies claiming 400% elongation after severe warm rolling [16]. Although the sample geometries used in these studies have been highly criticized for providing erroneously high tensile elongations [46], differences in grain boundary character produced by each processing pathway may also be a significant factor contributing to total tensile elongation. A thorough understanding of interplay between grain boundary structure and deformation mechanics is needed to explicitly determine the limits of low temperature superplasticity in sub-micron grained material. This work not only validates some of the early studies on non-equilibrium grain boundaries in severely deformed materials, but also provides rationale for future work in this area to further investigate the mechanistic limitations of low temperature superplasticity.

CONFLICTS

The authors declare that they have no conflict of interest.

ACKNOWLEDGEMENTS

The work herein is a part of the Center for Advanced Non-Ferrous Structural Alloys (CANFSA), a National Science Foundation (NSF) Industry-University Cooperative Research Center (IUCRC). The authors would like to thank J. Carpenter of Los Alamos National Laboratory (LANL) for his support in ARB studies and A. Creuziger of the National Institute of Standards and Testing (NIST) for his support in processing and representing texture data. The MTEX community served by R. Hielscher and R. Kilian have also been instrumental for collection and processing EBSD data.

REFERENCES

[1] A. J. Barnes: *J. Mater. Eng. Perform.*, 16(4):440-454, 2007.

[2] R. Koganti and J. Weishaar: *SAE Int. J. Mater. Manuf.*, 1(1):491-502, 2009.

[3] Hydro introduces new alloys for superplastic forming of complex automotive components. Light

Metal Age, pages 28-31, December 2018.

[4] A. J. Barnes, H. Raman, A. Lower, and D. Edwards: *Mater. Sci. Forum*, 735:361–371, 2013.

[5] J. Pilling and N. Ridley, *Superplasticity in crystalline solids*, Institute of Metals London, 1989.

[6] R. Verma, A. K. Ghosh, S. Kim, and C. Kim: *Mater. Sci. Eng. A*, 191(1-2):143-150, 1995.

[7] I. C. Hsiao and J. C. Huang: *Scr. Mater.*, 40(6):697-703, 1999.

[8] Y. Saito, H. Utsunomiya, N. Tsuji, and T. Sakai: *Acta Mater.*, 47(2):579-583, 1999.

[9] G. E. Totten and D. S. MacKenzie: *Handbook of Aluminum: Vol. 1: Physical Metallurgy and Processes*, Taylor & Francis, 2003.

[10] R. M. Cleveland, A. K. Ghosh, and J. R. Bradley: *Mater. Sci. Eng. A*, 351(1-2):228-236, 2003.

[11] A.K. Mukherjee, J.E. Bird, and J.E. Dorn: *Trans. ASM*, 62:155-179, 1969.

[12] M. Liu, R. Zheng, C. Ma, and N. Tsuji: *Mater.*, 8, 2019.

[13] J. C. Lee, S. H. Lee, S. W. Kim, D. Y. Hwang, D. H. Shin, and S. W. Lee: *Thermochim. Acta*, 499(1-2):100 105, 2010.

[14] F. Zhou, X. Z. Liao, Y. T. Zhu, S. Dallek, and E. J. Lavernia: *Acta Mater.*, 51:2777-2791, 2003.

[15] B. N. L. McBride, M. Sanders, K. D. Clarke, and A. J. Clarke, *Metall. Mater. Trans., A,* accepted July 2022.

[16] I. C. Hsiao and J. C. Huang. *Metall. Mater. Trans.. A*, 33A:1373-1384, 2002.

[17] B. N. L. McBride, K. D. Clarke, and A. J. Clarke: *J. Manuf. Process.*, 55:236-239, 2020.

[18] N. Tsuji, K. Shiotsuki, and Y. Saito: *Mater. Trans., JIM*, 40(8):765-771, 1999.

[19] N. Tsuji, R. Ueij, Y. Ito, and Y. Saito: *Proc. Risø Int. Symp. Metall. Mater. Sci.*, 607-616, 2000.

[20] I. C. Hsiao and J. C. Huang: *Scr. Mater.*, 40(6):697-703, 1999.

[21] ASTM E2448. ASTM International, West Conshohocken, PA, 2018.

[22] D. H. Bae and A. K. Ghosh: *Acta Mater.*, 48:1207-1224, 2000.

[23] R. Verma, P. A. Friedman, A. K. Ghosh, S. Kim, and C. Kim: *Metall. Mater. Trans. A*, 27:1889-1898, 1996.

[24] I. C. Hsiao, J. C. Huang, and S. W. Su: *Mater. Trans.*, 40(8):744-753, 1999.

[25] H. P. Pu, F. C Liu, and J. C. Huang: *Metall. Mater. Trans. A*, 26(5):1153-1166, 1995.

[26] Y. N. Wang and J. C. Huang: *Scr. Mater.*, 48(8):1117-1122, 2003.

[27] A. Gholinia, F. J. Humphreys, and P. B. Prangnell. *Acta Mater.*, 50:4461-4476, 2002.

[28] I. C. Hsiao, S. W. Su, and J. C. Huang: *Metall. Mater. Trans. A*, 31(9):2169-2180, 2000.

[29] X. Sauvage, G. Wilde, S. V. Divinski, Z. Horita, and R. Z. Valiev: *Mater. Sci. Eng. A*, 540:1-12, 2012.

[30] A. V. Mikhaylovskaya, O. A. Yakovtseva, I. S. Golovin, A. V. Pozdniakov, and V. K. Portnoy: *Mater. Sci. Eng. A*, 627:31-41, 2015.

[31] J. Lian, R. Z. Valiev, and B. Baudelet: *Acta Metall.*, 43(11):4165-4170, 1995.

[32] R. Z. Valiev, E. V. Kozlov, Y. F. Ivanov, J. Lian, A. A. Nazarov, B. Baudelet: *Acta Metall. Mater.*, 42(7):2467-2475, 1994.

[33] J. Weertman: *J. Appl. Phys.*, 28(10):1185-1189, 1957.

[34] A. H. Cottrell and M. A. Jason: *Proc. R. Soc. London*, 199(1056):104-114, 1949.

[35] E. M. Tale, G. A. Henshall, T. G. Nieh, D. R. Lesuer, and J. Wadsworth: *Metall. Mater. Trans. A,* 29(13):1081-1091, 1998.

[36] R. C. Gifkins: *Metall. Trans. A*, 7(8):1225-1232, 1976.

[37] A. K. Ghosh: *Mater. Sci. Forum*, 170172:39-46, 1994.

[38] X. Sauvage, N. Enikeev, R. Valiev, Y. Nasedkina, and M. Murashkin: *Acta Mater.*, 72:125-136, 2014.

[39] M. F. Ashby and R. A. Verrall: *Acta Metall.*, 21(2):149-163, 1973.

[40] T. G. Langdon: *Philos. Mag.*, 22(178):689-700, 1970.

[41] H. J. Frost and M. F. Ashby: *Deformation mechanism maps: the plasticity and creep of metals and Ceramics*, Pergamon Press, 1982.

[42] C. Herzig and S. V. Divinski: *Mater. Trans.*, 44(1):14-27, 2003.

[43] E. W. Hart: *Acta Metall.*, 15:351-355, 1967.

[44] A. J. Barnes: *J. Mater. Eng. Perform.*, 16(4):440-454, 2007.

[45] R Verma, P A Friedman, A K Ghosh, C Kim, and S Kim: *J. Mater. Eng. Perform.*, 4:543-550, 1995.

[46] F. Abu-Farha, M. Nazzal and R. Curtis: *Exp. Mech.*, 903-917, 2011.